Innate immune receptor NOD2 mediates LGR5$^+$ intestinal stem cell protection against ROS cytotoxicity via mitophagy stimulation

Antonin Levy[a,b,c,d,e], Aline Stedman[a,1], Eric Deutsch[b,c,d], Françoise Donnadieu[a], Herbert W. Virgin[f,2], Philippe J. Sansonetti[a,g,3], and Giulia Nigro[a,3]

[a]Molecular Microbial Pathogenesis Unit, Institut Pasteur, INSERM U1202, 75015 Paris, France; [b]Molecular Radiotherapy, INSERM U1030, Gustave Roussy Cancer Campus, Université Paris-Saclay, F-94805 Villejuif, France; [c]Department of Radiation Oncology, Gustave Roussy Cancer Campus, Université Paris-Saclay, F-94805 Villejuif, France; [d]Université Paris Sud, Université Paris-Saclay, F-94270 Le Kremlin-Bicêtre, France; [e]Ecole Doctorale Bio Sorbonne Paris Cité (BioSPC), Université Paris Diderot Paris 7, F-75205 Paris Cedex 13, France; [f]Department of Pathology and Immunology, Washington University School of Medicine, St. Louis, MO 63110; and [g]Chaire de Microbiologie et Maladies Infectieuses, Collège de France, 75231 Paris, France

Contributed by Philippe J. Sansonetti, July 23, 2019 (sent for review February 19, 2019; reviewed by Mathias W. Hornef, D. Brent Polk, and Marc Van de Wetering)

The nucleotide-binding oligomerization domain-containing protein 2 (NOD2) agonist muramyl dipeptide (MDP), a peptidoglycan motif common to all bacteria, supports leucine-rich repeat-containing G protein-coupled receptor 5 (LGR5)$^+$ intestinal stem cell (ISC) survival through NOD2 activation upon an otherwise lethal oxidative stress-mediated signal. However, the underlying protective mechanisms remain unknown. Here, using irradiation as stressor and primarily murine-derived intestinal organoids as a model system, we show that MDP induced a significant reduction of total and mitochondrial reactive oxygen species (ROS) within ISCs, which was associated with mitophagy induction. ATG16L1 knockout (KO) and NOD2 KO organoids did not benefit from the MDP-induced cytoprotection. We confirmed the MDP-dependent induction of ISC mitophagy upon stress in vivo. These findings elucidate the NOD2-mediated mechanism of cytoprotection involving the clearance of the lethal excess of ROS molecules through mitophagy, triggered by the coordinated activation of NOD2 and ATG16L1 by a nuclear factor κB (NF-κB)-independent pathway.

LGR5 intestinal stem cells | NOD2 | ROS | autophagy | muramyl dipeptide

In the gut epithelium, intestinal stem cells (ISCs) expressing leucine-rich repeat-containing G protein-coupled receptor 5 (LGR5) are located at the bottom of crypts and are actively cycling (1). The maintenance of LGR5$^+$ ISCs is essential for the regulation of an active epithelial repair following toxic and infectious injuries. These deleterious cytotoxic processes are largely mediated by the activation of the oxidative-stress machinery, leading to a massive production of reactive oxygen species (ROS) (2, 3).

Bacterial metabolites can control cell proliferation; for instance, butyrate has been shown to have an antiproliferative effect on ISCs (4). In addition, some microbe-associated molecular patterns (MAMPs) were shown to promote tissue repair through Toll-like receptors (TLRs) upon chemically induced damage (5), while lipopolysaccharide (LPS) from gram-negative bacteria induces a direct cytotoxic effect on ISCs through TLR4 signaling (6, 7). In contrast, as previously demonstrated by our group, the muramyl dipeptide (MDP)-nucleotide-binding oligomerization domain-containing protein 2 (NOD2) signaling pathway plays a cytoprotective role of ISCs, which express high levels of NOD2 transcripts. Cytoprotection was particularly prominent in ISCs subjected to the cytotoxic compound doxorubicin, a DNA-intercalating agent and promoter of excessive ROS production (8). However, the molecular and cellular mechanisms of cytoprotection downstream of MDP-NOD2 activation remain to be elucidated.

NOD2-mediated MDP sensing can initiate autophagy in specific immune cell types such as dendritic cells (9, 10). Autophagy is an evolutionarily conserved pathway that maintains cellular homeostasis by degrading damaged organelles, which includes mitochondria (mitophagy) in autophagosomes (11). Since mitochondria are a major source of intracellular ROS, alterations to mitophagy lead to elevated ROS levels (12, 13), thereby causing cytotoxicity that may significantly affect epithelial repair following ROS-inducing stress conditions.

In this study, using irradiation as a stressor in order to induce ROS-mediated LGR5$^+$ ISC cytotoxicity, we investigated if the MDP-NOD2 pathway of cytoprotection was mediated by activation of autophagy, thereby mitigating mitochondrial ROS release. Utilizing small intestinal organoids of wild-type (WT) and knockout (KO) mice (14), we found that MDP counteracts ISC

Significance

The intestinal epithelium represents the most vigorously renewing adult tissue in mammals. The renewal process is supported by the presence of intestinal stem cells (ISCs). Here we decipher a pathway of ISC cytoprotection mediated by a microbiota-derived product, the muramyl dipeptide (MDP). During stress conditions, recognition of MDP by the cytosolic sensor NOD2, which is expressed at high levels in ISCs, mediates the clearance of lethal excess of ROS molecules. The coordinated action of the autophagic protein ATG16L1 and NOD2 mediates the activation of a mitophagic process to eliminate damaged mitochondria and therefore protection of ISCs. We show a link between mitophagy-mediated ROS clearance and bacterial MDP stimulation in ISCs, therefore elucidating a role of the microbiota in epithelial regeneration.

Author contributions: P.J.S. and G.N. designed research; A.L., A.S., and F.D. performed research; H.W.V. contributed new reagents/analytic tools; A.L., E.D., P.J.S., and G.N. analyzed data; and A.L., P.J.S., and G.N. wrote the paper.

Reviewers: M.W.H., RWTH Aachen University; D.B.P., University of Southern California; and M.V.d.W., Prinses Máxima Centrum.

The authors declare no competing interest.

Data deposition: High-resolution versions of the figures are available on Figshare (DOI: 10.6084/m9.figshare.11536920).

[1]Present address: Developmental Biology Laboratory, CNRS UMR7622, INSERM U1156, Institut de Biologie Paris-Seine (IBPS), Sorbonne Universités, UPMC Univ Paris 06, F-75005 Paris, France.

[2]Present address: Vir Biotechnology, San Francisco, CA 94158.

[3]To whom correspondence may be addressed. Email: philippe.sansonetti@pasteur.fr or giulia.nigro@pasteur.fr.

This article contains supporting information online at https://www.pnas.org/lookup/suppl/doi:10.1073/pnas.1902788117/-/DCSupplemental.

First published January 9, 2020.

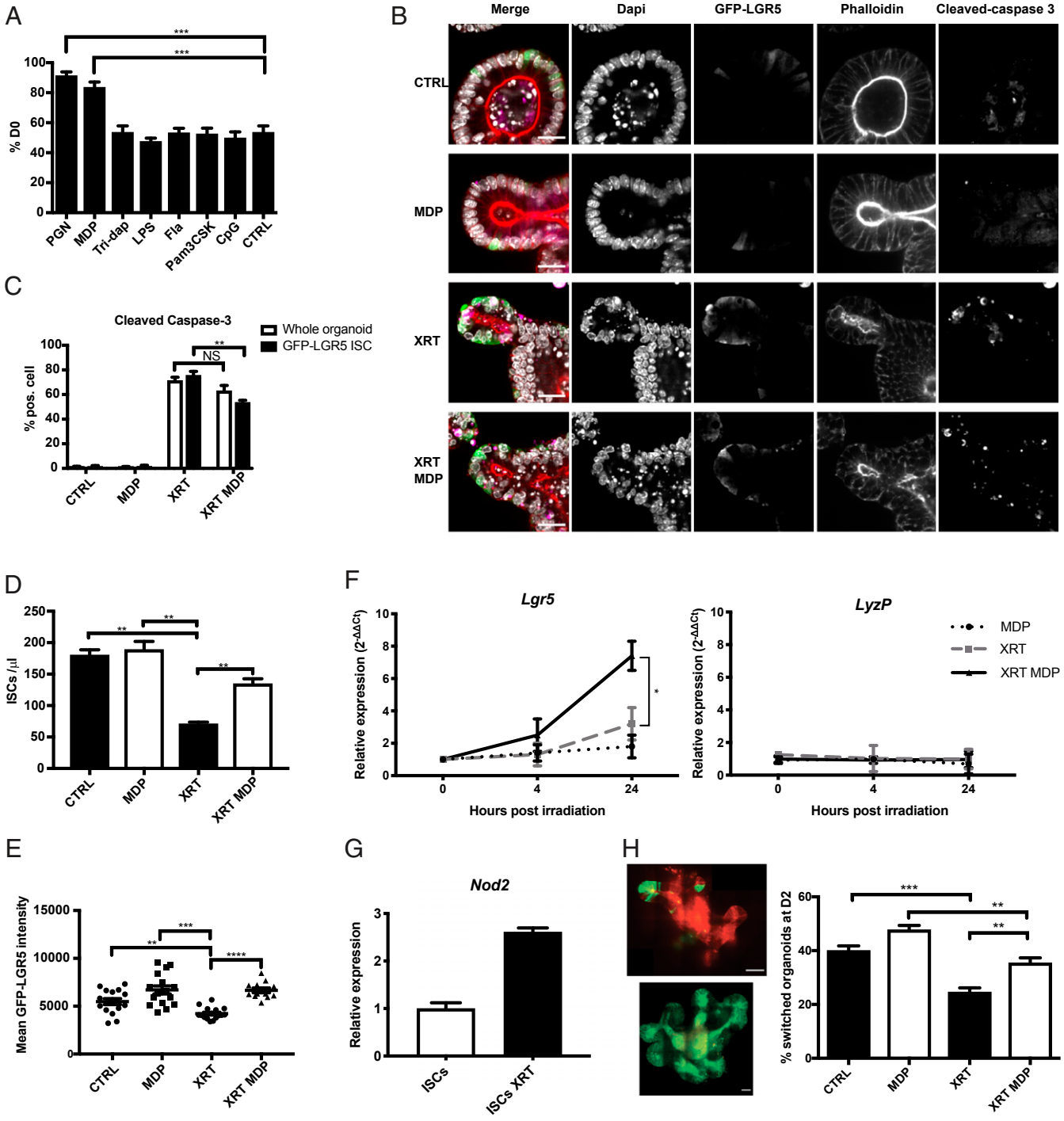

CELL BIOLOGY

Fig. 1. NOD2-MDP signaling pathway protects ISCs from stress in vitro. Organoids, grown with or without MDP, were analyzed after irradiation. (*A*) Percent of viable organoids 6 d upon XRT compared with the day of XRT (D0) in the presence or absence of PRR agonists. (*B*) Representative images of the budding site of organoids obtained from GFP-LGR5 mice (GFP-LGR5 ISCs in green) cultured in the presence or absence of MDP and/or 4 h after XRT and stained with anti-cleaved caspase-3 (magenta); DAPI (gray) and phalloidin (red). (Scale bar, 20 μm.) (*C*) The percentage of cleaved caspase-3–positive cells was scored in whole organoids and in GFP-LGR5 ISCs. (*D*) FACS quantification of GFP-LGR5 ISCs per microliter from MDP-stimulated and nonstimulated (CTRL) organoids 2 d (D2) after XRT. (*E*) Postacquisition image quantification of GFP-LGR5 ISC mean intensity per organoid (MDP-stimulated or not) at D2. (*F*) Gene expression level of *Lgr5* (*Left*) and *LyzP* (*Right*) with and without MDP on whole organoids 4 and 24 h after XRT. (*G*) Relative *Nod2* gene expression levels in ISCs sorted from irradiated organoids (upon 4 h) vs. ISCs sorted from nontreated organoids. (*H*) Representative images of GFP-LGR5;mTmG organoids after 2 d upon XRT cultured with (*Bottom*) or without (*Top*) MDP. 4-Hydroxytamoxifen (1 μM) was added the day of XRT. (Scale bar, 50 μm.) Percentage of organoids that switched entirely to cell membrane-localized GFP was measured at D2 after XRT. Data are represented as means ± SD. All conditions were performed in triplicate and images were acquired on at least 10 organoids per well ($n = 3$). Significant differences (Mann–Whitney *U* test): $^{**}P < 0.01$, $^{***}P < 0.001$, $^{****}P < 0.0001$; NS, not significant. See also *SI Appendix*, Figs. S1 and S3.

mitochondrial ROS by stimulating mitochondrial clearance via ATG16L1. In this context, ATG16L1 appeared to have a central role in the induction of mitophagy in addition to the blockage of nuclear factor κB (NF-κB) activity. These findings unravel a major protective mechanism of epithelial regeneration provided by the intestinal microbiota following chemical/physical, toxic, and possibly infectious aggression.

Results

MDP Selectively Protects LGR5$^+$ ISCs from Irradiation Damage and Enhances Epithelial Renewal. To elucidate the mediated effects of bacterial motifs on ISCs after irradiation (XRT), we cultured organoids from murine small intestinal crypts in the presence of purified or synthetic MAMPs. NOD receptors were stimulated by a soluble sonicated peptidoglycan (PGN) as a global NOD agonist, or a tripeptide containing *meso*-diaminopimelic acid (Tridap) and MDP as NOD1 and NOD2 agonists, respectively. Synthetic lipoprotein (Pam3CSK), *Escherichia coli* O111:B4 LPS, *Salmonella enterica* ser. Typhimurium flagellin (Fla), and synthetic unmethylated CpG dinucleotides (CpGs) were also tested to stimulate TLR2, TLR4, TLR5, and TLR9, respectively. In order to ensure the inclusion of MAMPs into the organoid lumen, the compounds were added to isolated crypts prior to embedding into Matrigel (*SI Appendix*, Fig. S1*A*). From the luminal compartment, MAMPs may directly interact with the apical TLRs and/or be transported into the cells through a transporter, such as SLC15A1 (PepT1) for the NOD ligands (15). Organoids were left to mature for 3 d of in vitro culture prior to subjection to an XRT dose–response study where 2 Gy was identified as optimal in order to induce an average of 50% lethality at day 6 post-XRT treatment. Thus, this irradiation dose was used for all of the subsequent experiments presented in this study (*SI Appendix*, Fig. S1*B*). Three days upon MAMP stimulation, the organoids were irradiated (D0) and the number of viable organoids was monitored 6 d after XRT. Upon stimulation with PGN and MDP, an increased number of surviving organoids was observed as shown by an increment of up to 33% in the presence of MDP and up to 41% in the presence of PGN as compared with nonstimulated organoids (control; CTRL). Interestingly, none of the other MAMPs had any effect on organoid survival, including the NOD1 agonist Tridap (Fig. 1*A*). The MDP-mediated protective effect was observed in organoids obtained from both WT and NOD1 KO mice but not present in those from NOD2 KO mice (*SI Appendix*, Fig. S1*C*), indicating a role of NOD2 independent of NOD1.

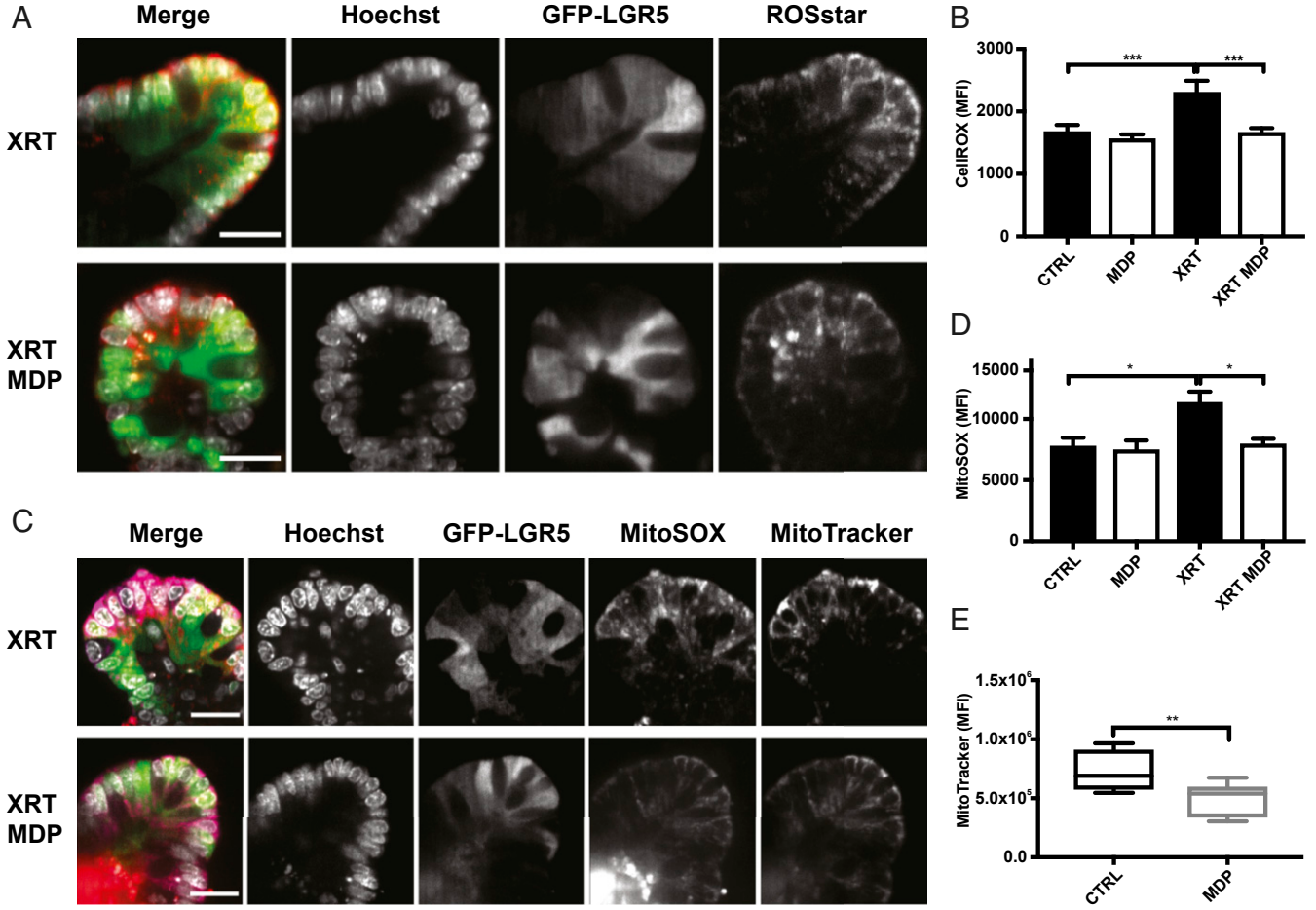

Fig. 2. MDP-NOD2 limit LGR5$^+$ ISC-ROS production. GFP-LGR5 organoids, grown with or without MDP, were analyzed for ROS production 1 h post XRT. (*A*) Images show representative staining of total ROS (ROSstar, in red) in irradiated organoids (ISCs in green and nuclei stained with Hoechst in gray). (Scale bars, 20 μm.) (*B*) Mean fluorescence intensity (MFI) of total ROS production (CellROX) in GFP-LGR5 ISCs. Black and white bars represent the absence or presence of MDP, respectively. (*C*) Representative images of mtROS- (mitoSOX, in red) and mitochondria- (MitoTracker, in magenta) stained irradiated organoids. Nuclei stained with Hoechst are in gray. (Scale bars, 20 μm.) (*D*) MFI of mitochondrial ROS production (using mitoSOX) in GFP-LGR5 ISCs obtained from dissociated organoids in gated ISCs (black and white bars represent the absence or presence of MDP, respectively) 1 h after XRT. (*E*) MFI of mitochondrial levels measured with MitoTracker on gated GFP-LGR5 ISCs. Data are represented as means ± SD. All conditions were performed in triplicate and images were acquired on at least 10 organoids per well ($n = 3$). Significant differences (Mann–Whitney *U* test): $^*P < 0.05$, $^{**}P < 0.01$, $^{***}P < 0.001$.

XRT has been shown to induce cell death via immediate apoptosis—primarily mediated by ROS production (16). To further assess if the effect of MDP is mediated via protection of LGR5$^+$ ISCs from XRT-induced apoptotic cell death, organoids from GFP-LGR5 mice were cultured with or without MDP, irradiated, and assessed for the induction of apoptosis 4 h post-stimuli. Independent of the stimulation (MDP and control), irradiation exhibited extensive epithelial apoptosis (positive for cleaved caspase-3) in whole organoids. In contrast, GFP-expressing LGR5$^+$ ISCs located at the budding site of the organoids (considered crypt-like domains; *SI Appendix*, Fig. S1*D*) presented a significantly lower number of cleaved caspase-3–positive events in the MDP-stimulated organoid group when compared with non-stimulated controls (Fig. 1 *B* and *C*). As reported in our previous analysis, no differences were observed in the maximal size of the organoids comparing stimulated and nonstimulated organoids, and

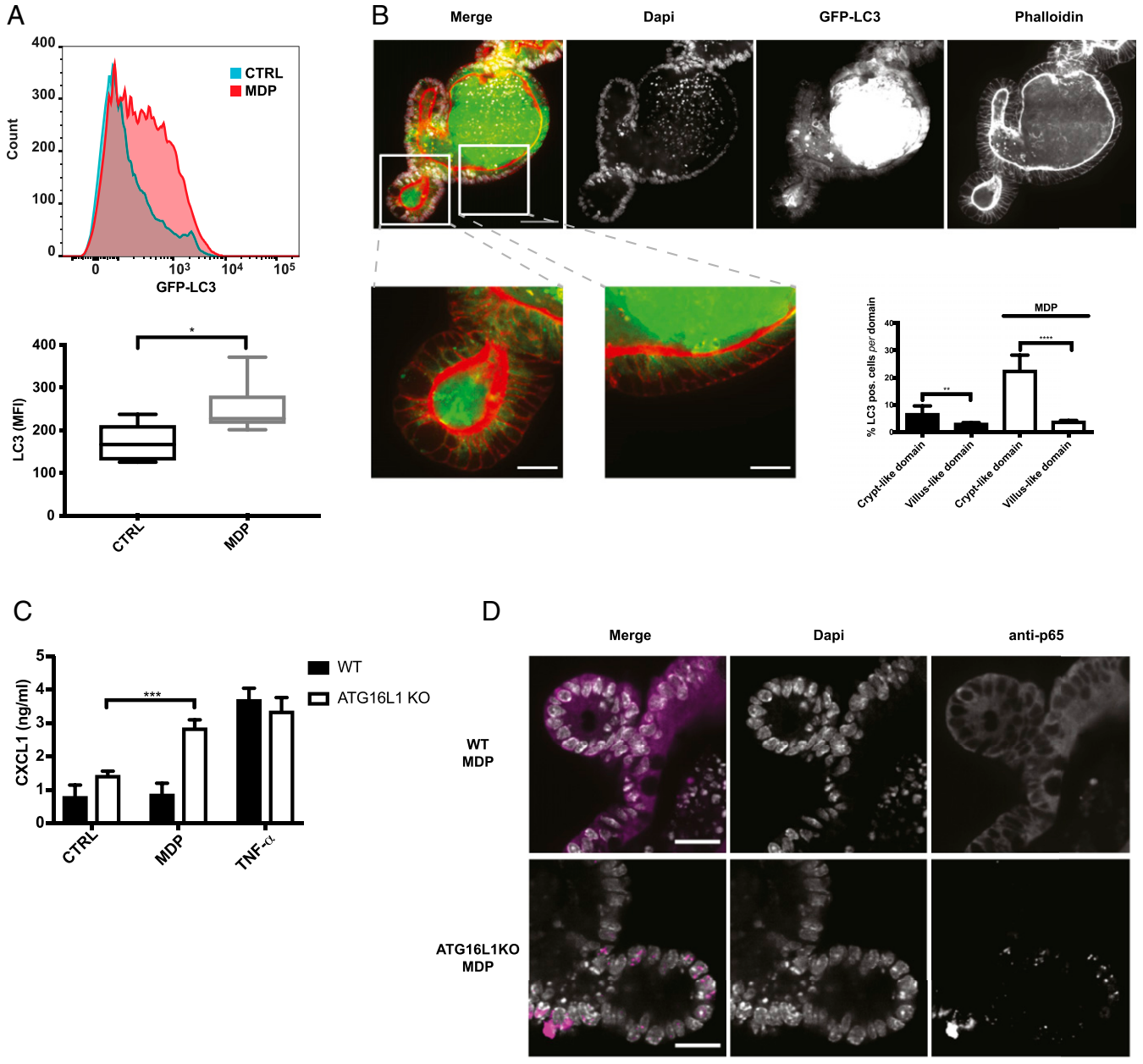

Fig. 3. MDP induces ISC autophagy but not NF-κB translocation in vitro. GFP-LC3 organoids, cultured with or without MDP, were analyzed for LC3 levels, in the absence of irradiation. (*A*) Representative flow cytometry histogram (*Top*) and MFI (*Bottom*) of LC3 levels in dissociated organoids. (*B*, *Top*) Representative images of organoids extracted from GFP-LC3 mice and cultured with MDP (nuclei are in gray, GFP-LC3 in green, and phalloidin in red). (Scale bars, 50 μm.) The boxes show a magnification of the crypt-like domain (*Bottom*, *Left*) and villus-like domain (*Bottom*, *Middle*). (Scale bars, 20 μm.) The graph is a quantification of the percentage of GFP-LC3–positive cells in crypt-like domains versus villus-like domains, in the presence or not of MDP. The activation of NF-κB was analyzed in WT and ATG16L1 organoids. (*C*) Quantification of CXCL1 production by ELISA from the culture supernatant of WT and ATG16L1 KO organoids stimulated or not with MDP. TNFα stimulation was used as positive control for CXCL1 production. (*D*) Representative images of anti-p65 staining (magenta) and nuclei (gray) in WT and ATG16L1 KO organoids upon MDP stimulation. (Scale bars, 20 μm.) Data are represented as % or means ± SD. All conditions were performed in triplicate and images were acquired on at least 10 organoids per well ($n = 3$). Significant differences (Mann–Whitney *U* test): $^*P < 0.05$, $^{**}P < 0.01$, $^{***}P < 0.001$, $^{****}P < 0.0001$. See also *SI Appendix*, Fig. S2.

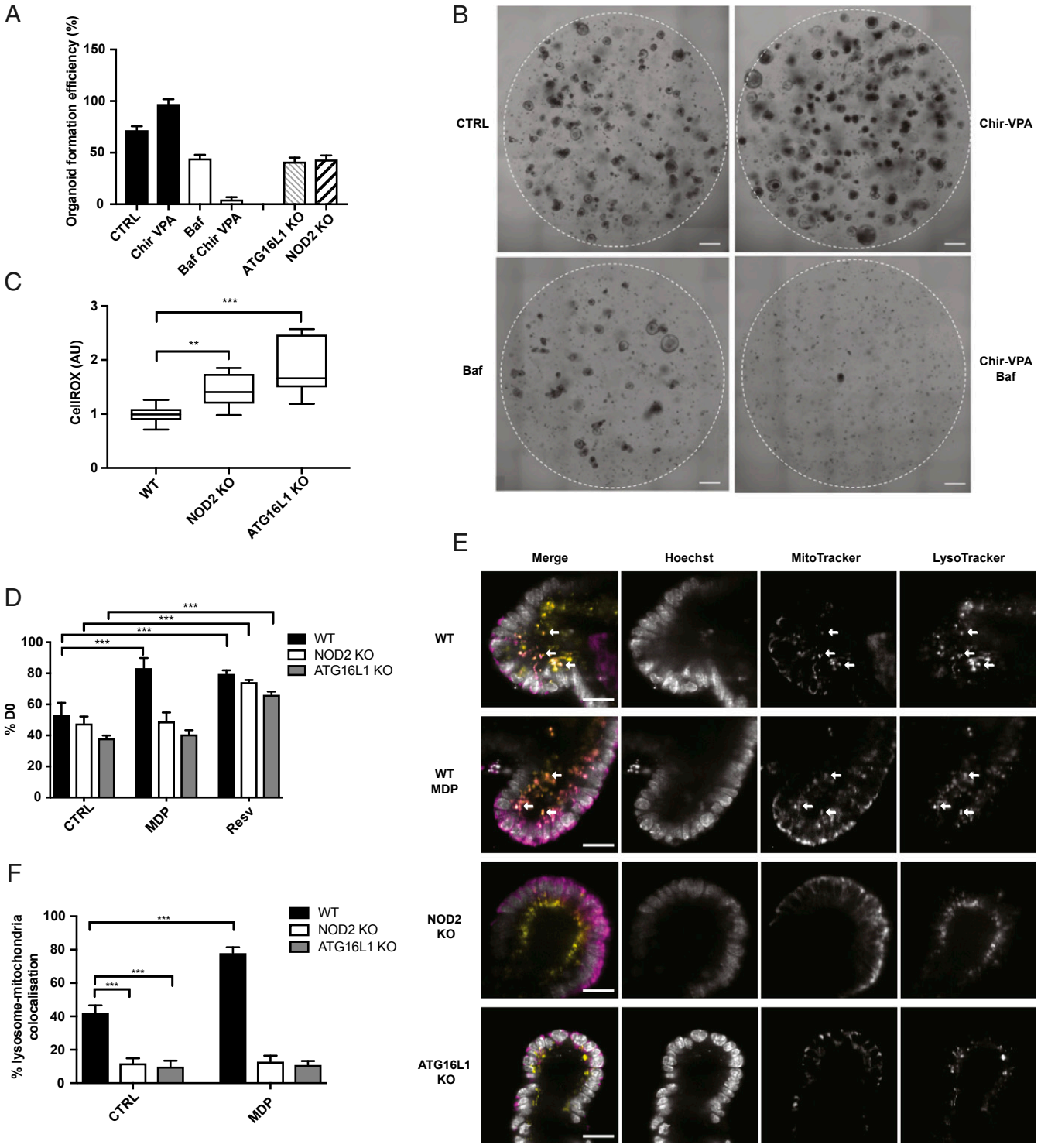

Fig. 4. Autophagy mediates LGR5^{+} intestinal stem cell cytoprotection. Crypts isolated from WT, NOD2 KO, and ATG16L1 KO mice were cultured for 7 d. Bafilomycin and/or CHIR99021-valproic acid was added to the culture media the day of plating. (*A*) Organoid-formation efficiency (%) equals the ratio of the number of living organoids counted on day 7 to the number of crypts seeded on day 0, in the absence of XRT. (*B*) Representative organoid culture on day 7 is shown. (Scale bars, 500 μm.) (*C*) Ratio of MFI of total basal (no XRT) ROS level (CellROX) on dissociated organoids obtained from NOD2 KO and ATG16L1 KO mice compared with WT organoids. (*D*) Crypts were extracted from WT, NOD2 KO, and ATG16L1 KO mice. Percent of viable organoids 6 d upon XRT compared with the day of XRT (D0) in the presence or absence of muramyl dipeptide or resveratrol (added just before XRT). (*E*) Representative confocal microscopy images of nonirradiated WT, NOD2 KO, or ATG16L1 KO organoids stained with LysoTracker (lysosomes in yellow), MitoTracker (mitochondria in magenta), and Hoechst (nuclei in gray). Arrows indicate colocalization of the 2 probes. (Scale bars, 20 μm.) (*F*) Quantification of lysosome–mitochondria colocalization obtained from the analysis of the images in *E*. Data are represented as % or means ± SD. All conditions were performed in triplicate and images were acquired on at least 10 organoids per well ($n = 3$). Significant differences (Mann–Whitney *U* test): $^{**}P < 0.01$, $^{***}P < 0.001$. See also *SI Appendix*, Fig. S2.

epithelial proliferation was also not affected by the presence of MDP (8).

To assess if the cytoprotective effect of MDP translated into an increase in the total LGR5$^+$ ISC pool, we quantified the number of LGR5$^+$ ISCs upon MDP stimulation in organoids generated from GFP-LGR5 mice. The concentration of LGR5-GFP cells (fluorescence-activated cell sorting [FACS] analysis) and the mean GFP fluorescence intensity (live imaging) were quantified 2 d following XRT (i.e., D2). Upon XRT, the number of LGR5-GFP cells was less than 50% compared with nonirradiated CTRL, while only a slight reduction was observed in the presence of MDP (Fig. 1*D*). This increased number of surviving ISCs in the presence of MDP was confirmed by measuring the GFP-LGR5 ISC mean intensity signal per organoid by confocal microscopy (Fig. 1*E* and *SI Appendix*, Fig. S1*D*). Further, gene expression analysis of whole organoids showed that the ISC marker (*Lgr5*) but not the Paneth cell (PC) marker (*LyzP*) was increased upon XRT in the presence of MDP (Fig. 1*F*). We then checked the gene expression levels of *Nod2* in sorted ISCs from organoids upon XRT vs. nonirradiated cells (sorting strategy in *SI Appendix*, Fig. S3*A*). Upon irradiation, *Nod2* was induced more than 2 times, suggesting a role for this receptor in LGR5$^+$ ISCs during a stress response (Fig. 1*G*). Collectively, these results show that MDP stimulation upon applied stress leads to protection of LGR5$^+$ ISCs in vitro.

To investigate this phenomenon further, we assessed if the presence of MDP allowed for LGR5$^+$ ISC-mediated epithelial renewal in organoids after irradiation. Lineage-tracing experiments were performed in organoids generated from GFP-LGR5;mTmG mice, in which LGR5$^+$ ISCs and their daughter cells express a membrane-bound red fluorescent tdTomato (mT) in their naïve state but switch to cell membrane-localized GFP (mG) expression upon 4-hydroxytamoxifen (4-OHT) induction. Organoids with entirely switched fluorescence from mT to mG, and therefore from red to green membranes (hereafter described as "switched" organoids), were counted at D2 (Fig. 1*H*). After XRT, MDP stimulation induced the switch of 35% of organoids (as in the CTRL condition) as compared with 20% in XRT alone, indicating that the MDP–NOD2 axis preserves LGR5$^+$ ISC numbers, enabling intestinal epithelial regeneration.

MDP Mitigates LGR5$^+$ ISC Mitochondrial ROS Levels. ISCs display high mitochondrial activity levels and it has been shown that oxidative metabolism is crucial for ISC proliferation and differentiation (17). Thus, at low levels, ROS is a component of important signaling pathways involved in the maintenance of normal cellular functions. At high levels, in contrast, ROS can be deleterious for cellular functions. XRT induces short-term water radiolysis and a high generation of ROS leading to both nuclear and mitochondrial DNA damage, disrupting mitochondrial functions (16). We examined whether MDP may limit the production of ROS in LGR5$^+$ ISCs after XRT in vitro. Intracellular ROS and mitochondrial ROS (mtROS) levels were monitored (by live microscopy) and quantified (by flow cytometry) using CellROX (cytosolic ROS staining) or ROSstar (a hydrocyanin-based probe of intracellular ROS staining) reagents and MitoSOX Red (mtROS staining) reagent, respectively. In GFP-LGR5 ISCs, total (Fig. 2 *A* and *B*) and mitochondrial (Fig. 2 *C* and *D*) ROS levels increased significantly 1 h after XRT in control organoids but not after MDP stimulation. Moreover, using MitoTracker Deep Red reagent, a reduction in the total amount of mitochondria was observed upon XRT in MDP-stimulated samples as compared with nonstimulated controls (Fig. 2 *C* and *E*). These results indicate the clearance of damaged mitochondria through activation of MDP-mediated mitophagy.

MDP-NOD2 Signaling Triggers ISC Autophagy but Not Inflammatory Immune Response. Upon pathogen invasion, NOD2 has a crucial role in the autophagic process by recruiting ATG16L1 to the plasma membrane and the induction of autophagosome formation (10, 18). To investigate if the observed reduction of mitochondria was due to the MDP-mediated activation of autophagy in ISCs, we generated organoids from GFP-LC3 mice and stimulated them or not with MDP. We quantified the activation of autophagy by measuring GFP-LC3 levels by flow cytometry (12) and counting GFP-LC3 puncta by confocal imaging. We showed an MDP-mediated increase in the GFP-LC3 signal in vitro (Fig. 3*A*), and most prominently in the crypt-like domain, where the LGR5$^+$ ISCs are located in comparison with the villus-like domain (Fig. 3*B*). Utilizing confocal imaging, we further confirmed that MDP induced autophagosomes, as identified by an anti-LC3B antibody, in LGR5$^+$ ISCs (*SI Appendix*, Fig. S2*A*).

We therefore assessed if NOD2-mediated autophagy was also associated with the induction of NF-κB and, consequently, the release of the proinflammatory cytokine CXCL1, which served as a bona fide marker of NF-κB activation. Following MDP stimulation, CXCL1 levels of WT organoids remained unchanged, while in ATG16L1 KO, we observed a 3-fold induction in cytokine production. Recombinant tumor necrosis factor alpha (TNFα), used as positive control, led to increased CXCL1 levels in both WT and ATG16L1 KO stimulated organoids (Fig. 3*C*). Similarly, in WT organoids, we did not detect nuclear translocation of the p65 subunit of the transcription factor NF-κB upon MDP stimulation in contrast to MDP-stimulated ATG16L1 KO organoids (Fig. 3*D*). These results demonstrate that ATG16L1 plays a central role in the activation of the autophagic machinery while inhibiting MDP-mediated NF-κB translocation. This dissociation of the NOD2-mediated innate immune response is likely due to ATG16L1 serving as a negative regulator of the NOD2-driven activation of the RIP2 pathway which activates NF-κB.

Autophagy Mediates LGR5$^+$ ISC MDP-NOD2–Induced Cytoprotection. To study whether autophagy was involved in the observed ISC regeneration, we evaluated the crypts' potential for intestinal epithelial regeneration in vitro by utilizing a crypt-organoid–formation assay. The organoid-formation capacity of the crypts from both ATG16L1 KO and NOD2 KO mice was significantly reduced compared with those from WT mice (Fig. 4*A* and *SI Appendix*, Fig. S2*B*), suggesting that stress induced by crypt extraction was sufficient to activate the autophagic protective pathway in the WT. To explore if this effect was specific to ISCs, we artificially increased the number of ISCs per organoid. Wnt3 and Notch signals are essential for intestinal epithelial stemness (19). The combination of CHIR99021 (Chir; a GSK3β inhibitor that activates the Wnt pathway) and valproic acid (VPA; a histone deacetylase [HDAC] inhibitor that activates Notch) increased organoid-formation efficiency and maintained LGR5$^+$ ISCs in an undifferentiated, self-renewing state (20) (*SI Appendix*, Fig. S2*C*). The addition of 100 nM bafilomycin A1 (an autophagy inhibitor) to the crypt media decreased organoid-formation capacity, similar to extracted crypts from both ATG16L1 KO and NOD2 KO mice, and dramatically decreased the organoid-formation capacity in Chir-VPA–treated WT organoids (Fig. 4 *A* and *B*). These results indicated that the lack of autophagy is more deleterious to ISCs than to differentiated cells.

To evaluate if the lack of autophagy was associated with the increased levels of cytotoxic ROS, we evaluated the amount of intracellular ROS in organoids generated from both NOD2 KO and ATG16L1 KO mice. We observed significantly higher levels in both KO when compared with WT organoids under steady-state conditions (Fig. 4*C*). To assess the impact of ATG16L1 on balancing ROS levels, and therefore its importance in ISC cytoprotection, we tested the survival of ATG16L1 KO organoids upon stress. Six days after XRT, MDP stimulation no longer increased the number of surviving ATG16L1 KO organoids. Since high ROS levels mediate XRT cytotoxicity (16), we tested whether the survival capacity of organoids could be restored by treatment

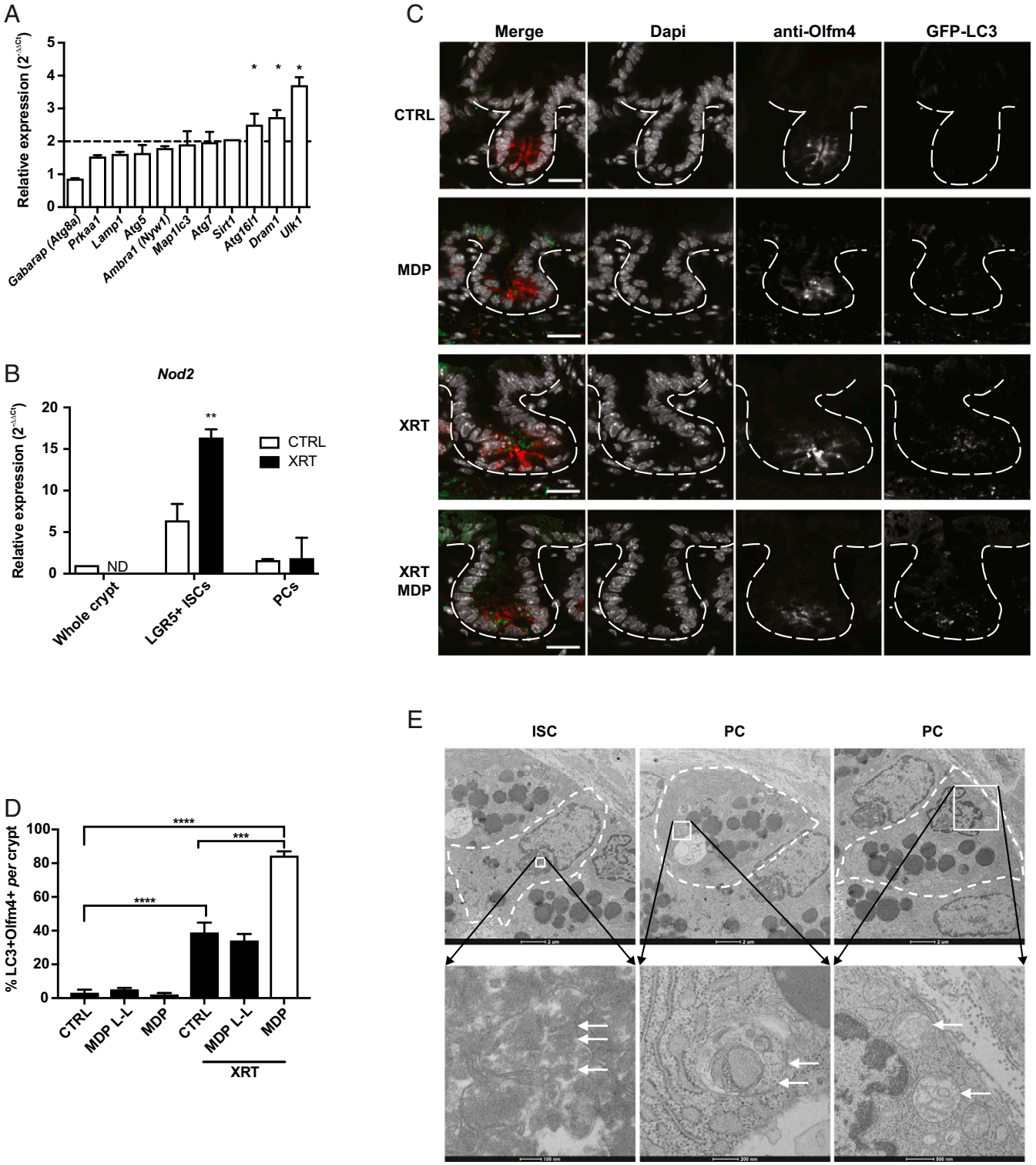

Fig. 5. MDP promotes LGR5^{+} intestinal stem cell mitophagy after stress in vivo. The ISCs of mice treated or not with XRT were analyzed. (*A*) Basal gene expression levels of autophagy-related genes in LGR5^{+} ISCs as compared with whole epithelial crypt cells. (*B*) *Nod2* expression levels in sorted intestinal stem cells and Paneth cells from mice 4 h after XRT or from control mice. Data are normalized to RNA basal expression levels from whole epithelial crypt cells. (*C*) Images show representative anti-Olfm4 (in red) staining (ISCs) in the crypts of GFP-LC3 mice (LC3 in green) 4 h after XRT in the presence or absence of MDP (nuclei in gray). (Scale bars, 20 μm.) (*D*) The percentage of ISCs (stained with anti-Olfm4) that displayed GFP-LC3 puncta ("positive cells") per crypt after XRT in the presence of MDP, MDP L-L (L-L isomer, inactive), or nontreated control was scored. (*E*) Morphology of ISCs and PCs of MDP-treated mice 4 h after XRT was analyzed by transmission electron microscopy. Examples of mitochondria are shown in the square and in the enlarged (*Bottom*) panels (arrows). Mitophagy was observed in ISCs (*Left*) but not in PCs (*Middle* and *Right*). Autophagosome formation and altered mitochondria were observed in PCs (*Middle*) but not mitophagy. Data are represented as means ± SD. Significant differences (Mann–Whitney *U* test): $^{*}P < 0.05$, $^{**}P < 0.01$, $^{***}P < 0.001$, $^{****}P < 0.0001$. See also *SI Appendix*, Fig. S3.

with the antioxidant resveratrol (Resv), known to affect mtROS in vitro (21). Upon treatment with Resv, the number of surviving organoids obtained from WT, NOD2 KO, and ATG16L1 KO mice was partially restored (Fig. 4*D*).

To verify if MDP may activate mitophagy by induction of ATG16L1 also without XRT, we checked for lysosome–mitochondria (autophagosome) association, as assessed by LysoTracker and MitoTracker, respectively. After MDP stimulation, we observed an increase in lysosome–mitochondria association, consistent with ATG16L1 recruitment by NOD2 and subsequent mitophagy activation. Conversely, NOD2 KO and ATG16L1 KO organoids exhibited defects in lysosome–mitochondria colocalization in both control and MDP-stimulated conditions, suggesting impairment of the mitophagy process (Fig. 4 *E* and *F*). Taken together, these results indicate that MDP induces NOD2/ATG16L1 activation, leading to mitophagy and therefore balancing intracellular ISC ROS levels.

MDP Induces Intestinal Stem Cell Mitophagy after Irradiation in Vivo. To check for the presence of genes associated with the autophagic machinery in ISCs, we performed expression analyses of a panel of autophagy-implicated genes on sorted ISCs from GFP-LGR5 mice (the sorting strategy is in *SI Appendix*, Fig. S3*A*). We found an up-regulation of autophagy-pathway genes in ISCs as compared with whole epithelial crypt cells, including *Atg16L1* and *Ulk1* (Unc-51–like kinase 1), a downstream P-AMPK–activated autophagy-initiating kinase (Fig. 5*A*). Moreover, upon XRT, we observed that the *Nod2* gene was the highest-induced pattern recognition receptor (PRR) in ISCs, while no change was detected in PCs, confirming our observations in vitro (Fig. 5*B* and *SI Appendix*, Fig. S3*B*).

To assess if MDP induces ISC autophagy in vivo, GFP-LC3 mice were subjected to antibiotic treatment to deplete the intestinal microbiota and MDP was administered before total-body irradiation. Four hours after XRT, we observed an MDP-mediated increase in GFP-LC3 puncta within ISCs, stained with anti-Olfm4 antibody (Fig. 5 *C* and *D*). MDP, and not its inactive isomer MDP L-L, in the absence of XRT did not induce ISC autophagy in vivo, confirming that the cytoprotective signal is primarily activated upon stress.

To confirm the MDP-mediated induction of ISC mitophagy upon oxidative stress, we analyzed intestinal tissues by transmission electron microscopy (TEM) (Fig. 5*E*). We identified ISCs as lateral neighbors of PCs, located at the bottom of the crypts. In ISCs of MDP-treated, irradiated mice, we observed vacuoles filled with contents of different electron density corresponding to autolysosomes. These vacuoles were surrounded by a single membrane and part of the content had an amorphous appearance. Inside these vacuoles, we found remnants of mitochondria characterized by the presence of cristae (Fig. 5 *E*, *Left*). By contrast, the same treatment induced a drastic morphological change to the mitochondria of PCs (Fig. 5 *E*, *Right*). Compared with untreated tissue (*SI Appendix*, Fig. S3*C*), mitochondria of PCs displayed disarrangement of cristae and the mitochondrial lumen showed signs of extraction and the presence of membrane swirls. Despite morphological changes in PC mitochondria, no degradative compartments comprising mitochondria were observed. However, profiles of early autophagosomes were present in the cytosol of PCs (Fig. 5 *E*, *Middle*), characterized by the presence of membranes and ribosomes in the lumen and surrounded by a double membrane with the outer membrane devoid of ribosomes on its cytosolic side.

Discussion

We previously demonstrated in mice that the cytosolic receptor NOD2 is highly and uniquely expressed in ISCs, as opposed to all other members of the epithelial lining. We further showed that the presence of its MDP agonist, a universal building block of the bacterial cell wall, significantly protects ISCs upon doxorubicin-induced stress (ROS production) (8). Combining in vivo and ex vivo experiments utilizing intestine-derived organoids, this work established evidence for the involvement of an intestinal microbiota-associated bacterial motif in epithelial regeneration. This is regulated by MDP-induced modulation of stem cell viability and by a cytoprotective process involving the NOD2 pathway. Up to now, NOD2 has been primarily implicated as a component of the innate, NF-κB–dependent, proinflammatory immune response to bacterial pathogens, as immune cells, such as macrophages and dendritic cells, are generally recognized as bona fide producers of NOD2 (22). However, a more recent publication suggests an alternative signaling route involving NOD2 and the autophagy effector ATG16L1, leading to an autophagy-mediated increase of the class II antigen presentation of bacteria-infected antigen-presenting cells (9).

In any event, the key molecular mechanism involved in MDP-NOD2–mediated cytoprotection of ISCs had not yet been addressed. Hence, we established and validated an irradiation stress model of murine small intestinal organoids in order to decipher the signaling chain involved in cytoprotection. Here we show an alternative route of NOD2 signaling, comprising the active down-regulation of NF-κB, to favor a pathway in which MDP activation of NOD2 leads to ATG16L1 engagement and autophagy stimulation. Autophagy in this context is primarily dominated by mitophagy, allowing for the sequestration of damaged mitochondria, which were identified as major ROS producers upon irradiation stress in ISCs.

Asano et al. (23) found that intrinsic autophagy is important for the maintenance of ISCs by reducing excessive ROS. This stem cell maintenance was necessary to provide damage-induced intestinal regeneration after an oxidative stress such as irradiation. Along similar lines, caloric restriction-induced autophagy (via mTOR inactivation) increased the numbers of $LGR5^+$ ISCs and simultaneously promoted the survival and regeneration of intestinal crypts following exposure to radiation (24). Fasting also preserved ISCs following a strong oxidative stress with chemotherapy (25). Altogether, these studies suggest that autophagy could be implicated in ISC cellular homeostasis upon stress. It is therefore possible that XRT alone partly induces ISC autophagy due to strong ROS production.

Low-grade mitochondria-derived ROS is essential for ISC maintenance, proliferation, and differentiation; however, in excess, ROS triggers p53-mediated ISC death (17, 26). This implies the existence of a "gray zone," where physiological ROS concentrations allow for stem cell maintenance and function while an excessive ROS concentration results in cytotoxicity. This work unravels a fascinating angle of host–microbiota symbiosis whereby coevolution has harnessed NOD2, a microbial danger sensor (22), and ATG16L1, a key regulator of autophagosome maturation (27, 28), to control ROS levels to this sensitive gray zone during ISC stress. On the one hand, reducing ROS levels helps to preserve ISC survival, thereby having a positive impact on epithelial regeneration upon immediate stress conditions including infection, exposure to food toxins, nutritional factors, and xenobiotics. On the other hand, long-term events, like in the case of intestinal dysbiosis, may alter the symbiotic balance and lead to deficient provision of MDP, and thus to delayed epithelial repair following alteration. This hypothesis is supported by the dominance of NOD2 and ATG16L1 "loss-of-function" polymorphisms among the numerous polymorphisms identified in Crohn's disease patients by genome-wide association studies in patients suspected of a genetically transmitted trait (29). Alternatively, excessive expression of this symbiotic function may alter ISC "quality control" and prevent p53-mediated cell death, which may result in the dangerous accumulation of somatic mutations upon stress-induced DNA breaks and the increased risk for cancer stem cell development (30). This emphasizes the urgent need for technological

breakthroughs allowing for the measurement of MDP concentrations in intestinal crypts at homeostasis and in pathological conditions. Taken together, in the ISCs, NOD2 stimulation with MDP results in the activation of the autophagic pathway as opposed to the canonical induction of cytokines, chemokines, and antimicrobial genes.

Due to their location, ISCs are more protected from invasive bacteria when compared with other epithelial cells. Moreover, additional PRRs are still expressed by ISCs, including NOD1. Therefore, we could hypothesize that in ISCs, NOD2 has a shift of function, representing a receptor responding to "good" stimuli from commensal bacteria to counter stress signals, while NOD1 mediates host–pathogen responses.

In this study, we show a link between mitophagy-mediated ROS clearance and bacterial MDP stimulation in ISCs, thereby linking microbiota and epithelial regeneration (*SI Appendix*, Fig. S4). This may provide a novel angle to understanding the pathophysiology of Crohn's disease and new prospects for translation into clinical practice for patients receiving oxidative-generating anticancer agents.

Methods

Mice. Lgr5-EGFP-IRES-CreERT2 (GFP-LGR5) mice were purchased from The Jackson Laboratories. *Card15*/*Nod2*-deficient C57BL/6J (NOD2 KO) mice were provided by J.-P. Hugot, Hôpital Robert Debré, Paris, France (31). GFP-LGR5 mice were crossed with ROSA$^{mT/mG}$ (mTmG) Cre reporter mice (provided by Institut Pasteur) (32) to obtain GFP-LGR5;mTmG mice. C57BL/6N ATG16L1$^{flox/flox}$*villin-Cre* (ATG16L1 KO) mice were provided by H.W.V. (33) and C57BL/6J-Tg(CAG-EGFP/Map1lc3b)53Nmz (GFP-LC3) tg mice (34) were provided by Institut Pasteur. In each experiment, age- and sex-matched mice were used as controls and were nonlittermates in some experiments. All mice were kept under specific pathogen-free conditions and all animal experiments were carried out under approval by the Animal Care and Use Commitee of Institut Pasteur and by the French Ministry of Agriculture (2016-0022). For the detection of ROS generation, mice were given a single i.p. injection of 100 μL 12.5 μM ROSstar 550 (Li-Cor) for 30 min. The depletion of the microbiota was performed as previously described (8, 35). Briefly, water flasks were supplemented with 1 g/L ampicillin (Sigma) and mice were gavaged every day for 10 d with 200 μL of a freshly made mixture of the following antibiotics: 10 mg/mL metronidazole (Sigma), 5 mg/mL vancomycin (Acros), 5 mg/mL neomycin (Sigma), and 0.1 mg/mL amphotericin B (Pan-Biotech).

Five days before irradiation, 100 μM MDP or inactive MDP L-L isomer (InvivoGen) was added to the drinking water (50 μg/mL) and 200 μg of the specific compounds was given daily by gavage. For all experiments at least 5 animals per condition were used.

Crypt Isolation and Organoid Formation. Intestinal crypts were extracted as previously described (8). The intestines were flushed and treated with bleach to remove any possible contamination from the luminal bacteria. To ensure MAMP enclosure into the organoids, lumen and size homogeneity organoid assays were always performed from isolated crypts. Two hundred and fifty crypts (generating roughly 150 organoids) were centrifuged and the following MAMPs were added or not and let stand for 10 min at room temperature before embedding: 10 μg/mL soluble sonicated peptidoglycan from *E. coli* K12 (PGN), 10 μg/mL *N*-acetylmuramyl-L-alanyl-D-isoglutamine (MDP), 10 μg/mL lipopolysaccharide from *E. coli* O111:B4, 500 ng/mL lipoprotein (Pam3), 10 ng/mL *S. enterica* ser. Thyphimurium flagellin, 1 μM synthetic unmethylated CpG dinucleotides, or 10 μg/mL L-Ala-γ-D-Glu-mDAP (Tridap) (all from InvivoGen). The crypts were then embedded in 30 μL growth factor-reduced Matrigel (Corning), seeded in 48-well plates, incubated for 20 min at 37 °C, and overloaded with 300 μL of crypt medium as previously described (8). The medium was exchanged every 4 d. If needed, medium was supplemented with CHIR99021 (3 μM; Stemgent) and valproic acid (1 mM; Sigma-Aldrich) over the course of 72 h to enrich organoids with stem cells (20). Organoids were recovered using Cell Recovery Solution (Corning) at 4 °C for 15 min to dissolve the Matrigel, followed by 3 washes of the pelleted cells with phosphate-buffered saline (PBS). 4-Hydroxytamoxifen (1 μM; Sigma-Aldrich) was added in GFP-LGR5;mTmG crypt media to induce activation of CreERT2 and consequently excision of the tdTomato-pA cassette (36).

Flow Cytometric Analysis and Sorting. Isolated crypts from GFP-LGR5 mice were incubated in HBSS without Ca^{2+} and Mg^{2+} supplemented with 0.3 U/mL Dispase (Corning), 0.8 U/μL DNase (Sigma), and 10 μM Y-27632 (Sigma) for 30 min at 37 °C. For cell sorting, dissociated cells were washed with 1% BSA/PBS and stained with CD24-APC antibody (1:20; BioLegend; M1/69) and EpCam Pe-Cy7 (1:100; BioLegend; G8.8) for 20 min at 4 °C. The cells were then resuspended in crypt media supplemented with 10 μM Y-27632, filtered with a 35-μm mesh, and analyzed by MoFlo Astrios (Beckman Coulter). Sorted cells were collected in RLT buffer (Qiagen). For flow cytometric analysis, GFP-LGR5 or ATG16L1 KO organoids were removed from the Matrigel with Cell Recovery Solution (Corning), dissociated with Dispase solution (as for the isolated crypts), stained, and acquired on a FACSCanto II (BD Biosciences) or an Attune NxT flow cytometer (Thermo Fisher) and analyzed by FlowJo software (Tree Star). GFP-LGR5 ISC concentration was measured using CountBright absolute counting beads (Thermo Fisher).

Real-Time PCR. Total RNA was extracted with the RNeasy Mini or Micro Kit (Qiagen) and the complementary (c)DNA was made with SuperScript II Reverse Transcriptase (Thermo Fisher) and oligo(dT)12 to 18 primer (Thermo Fisher) as recommended by the suppliers. The primers (Bio-Rad) and probes (TaqMan Assays; Thermo Fisher) are listed in *SI Appendix*, Table S1. Reactions were run on a QuantStudio 7 (Thermo Fisher) using Power SYBR Green Master Mix (Thermo Fisher) or TaqMan Universal PCR Master Mix (Thermo Fisher) according to the manufacturer's instructions. For GFP^{high}CD24^{middle} sorted-cell gene expression analysis, 20 ng of cDNA from each condition was preamplified using the TaqMan Preamp Master Mix Kit (Thermo Fisher). After preamplification, samples were diluted 1:20 before high-throughput microfluidic real-time PCR analysis. Amplified cDNA samples were assayed for gene expression using individual real-time (RT)-PCR primers and 96.96 dynamic arrays on a BioMark System by following the manufacturer's protocol (Fluidigm). Beta2-microglobulin was used as a housekeeping gene and $2^{-\Delta\Delta Ct}$ (cycle threshold) values were calculated to obtain relative expression as compared with RNA extracted from whole epithelial crypt cells.

Radiation. For the irradiation-injury studies, organoids (in vitro XRT) received 2 Gy with exception of the incremental irradiation doses (*SI Appendix*, Fig. S1) and mice (in vivo XRT) received 12-Gy whole-body irradiation using an Xstrahl 320 irradiator (Camberley). Mice were euthanized 4 h after treatment.

Imaging Detection. For confocal laser-scanning microscopy, the organoids or the tissue was fixed and embedded in agarose or in OCT compound 4583 (Sakura) as already described (37). Sections of 150 μm (agarose) or 10 μm (OCT) were obtained by using an HM650V vibratome (Thermo Fisher) or a CM3050S cryostat (Leica), respectively. For antigen retrieval, slides were steamed for 20 min in 10 mM citrate buffer (pH 6) and cooled for 30 min. Rabbit anti-cleaved caspase-3 (1:100; Cell Signaling Technology; Asp175), chicken anti-GFP (1:500; Abcam; ab13970), rabbit anti-LC3B (1:200; Abgent; AP1802a), rabbit anti-p65 (1:100; Abcam; 7970), mouse anti-Olfm4 (1:200; Cell Signaling Technology; D6Y5A), phalloidin 568 (Thermo Fisher), and corresponding secondary antibodies (Alexa Fluor 488, 568, or 647; Thermo Fisher) were used. DNA was stained by DAPI (1 μg/mL; Thermo Fisher). The sections were mounted with ProLong Gold Antifade Reagent (Thermo Fisher). Images were acquired using an IX-81 (Olympus) or Opterra swept-field confocal microscope (Bruker) equipped with thermic chamber and CO_2 control. Postacquisition image analysis was performed with Fiji 2.0.0 software.

Measurement of Intracellular ROS. Total intracellular ROS and mitochondrial ROS were measured by flow cytometry (cf. *Flow Cytometric Analysis and Sorting* above; the dye was added after dissociation) or live imaging. For total ROS, CellROX Deep Red (2.5 μM, 30 min at 37 °C; Thermo Fisher) and ROSstar 550 (2.5 μM, 30 min at 37 °C; Li-Cor) were used. For mtROS, MitoSOX Red (5 μM for 30 min at 37 °C; Mitochondrial Superoxide indicator; Molecular Probes) was used. For live imaging, DNA was stained with Hoechst 33342 (20 μM; Thermo Fisher) and cells were washed with DMEM FluoroBrite (Gibco). Resveratrol (40 μM; Sigma) was used as an antioxidant agent and directly added to the culture media just before irradiation and during subsequent culture.

Autophagy and Mitophagy Analyses. Live organoids were incubated for 30 min at 37 °C in the dark with 50 nM MitoTracker Deep Red and/or 50 nM LysoTracker (both from Thermo Fisher). DNA staining and washes were performed as described above. Bafilomycin A1 (Sigma) was added to the culture media for organoid-formation efficiency tests at a concentration of 100 nM as determined by a dose–response study (*SI Appendix*, Fig. S2*D*).

Increased LC3 concentration on the membrane provided a stronger signal, as was previously reported (12). Images of GFP-LC3 sections were collected using confocal microscopy. The *z*-stack images were collected and the GFP signals were analyzed through the sections. Using Fiji, the percentage of LC3-GFP–positive cells on different organoid domains (crypt-like versus villus-like domains) was assessed (Fig. 3*B*).

Transmission Electron Microscopy. Mice were euthanized, the intestine was extracted, and small pieces were fixed by immersion in 2.5% glutaraldehyde (EMS) in PHEM buffer (pH 7.2) at room temperature. Samples were postfixed with 1% osmium tetroxide + 0.8% ferricyanide in 0.1 M cacodylate buffer (pH 7.2) and dehydrated by an ethanol series followed by propylene oxide before gradual infiltration with EPON resin. After heat polymerization, thin sections were cut and picked up on carbon/formvar-coated slot grids. Images were taken with a Tecnai G2 microscope operated at 120 kV equipped with a Gatan US 4000 CCD camera.

ELISA. Murine CXCL1 assays were performed according to the manufacturer's protocols (R&D Biosystems; DY453-05). After 3 d of organoid culture, XRT or recombinant murine TNFα (100 ng/mL; PeproTech) (used as positive control) was applied, and the supernatant was recovered after 24 h (at D4).

Statistical Analysis. The descriptive statistical analysis was performed with Prism version 7 (GraphPad Software). Results are expressed as means ± SD of at least $n = 3$ replicates. Statistical comparisons were performed using the Mann–Whitney U test. $P < 0.05$ was considered significant.

Data Availability. All relevant data, associated protocols, and materials are within the manuscript and its *SI Appendix* files. If any additional information is needed, it will be available upon request from the corresponding authors.

ACKNOWLEDGMENTS. We acknowledge the Center for Translational Science (CRT)-Cytometry and Biomarkers Unit of Technology and Service (CB UTechS) at Institut Pasteur, and particularly P. H. Commere, for support in conducting the cell sorting. We acknowledge the Ultrastructural BioImaging Unit and particularly M. Sachse for his help and support with TEM. We thank Katja Brunner for critical reading of the manuscript. This work was supported by European Research Council Advanced Grant 339579-DECRYPT (to P.J.S.) and French National Research Agency (ANR) Grant 17-CE14-0022 (i-Stress) (to P.J.S.). A.L. was funded by Poste d'Accueil INSERM, and Soutien pour la Formation à la Recherche Translationnelle en Cancérologie (ITMO Cancer, INCa-Plan Cancer 2014–2019, Allocation ASC17040JSA).

1. N. Barker *et al*., Identification of stem cells in small intestine and colon by marker gene Lgr5. *Nature* **449**, 1003–1007 (2007).
2. G. Hua *et al*., Distinct levels of radioresistance in Lgr5$^+$ colonic epithelial stem cells versus Lgr5$^+$ small intestinal stem cells. *Cancer Res.* **77**, 2124–2133 (2017).
3. C. Metcalfe, N. M. Kljavin, R. Ybarra, F. J. de Sauvage, Lgr5$^+$ stem cells are indispensable for radiation-induced intestinal regeneration. *Cell Stem Cell* **14**, 149–159 (2014).
4. G. E. Kaiko *et al*., The colonic crypt protects stem cells from microbiota-derived metabolites. *Cell* **165**, 1708–1720 (2016).
5. S. Rakoff-Nahoum, J. Paglino, F. Eslami-Varzaneh, S. Edberg, R. Medzhitov, Recognition of commensal microflora by Toll-like receptors is required for intestinal homeostasis. *Cell* **118**, 229–241 (2004).
6. T. Naito *et al*., Lipopolysaccharide from crypt-specific core microbiota modulates the colonic epithelial proliferation-to-differentiation balance. *MBio* **8**, e01680-17 (2017).
7. M. D. Neal *et al*., A critical role for TLR4 induction of autophagy in the regulation of enterocyte migration and the pathogenesis of necrotizing enterocolitis. *J. Immunol.* **190**, 3541–3551 (2013).
8. G. Nigro, R. Rossi, P.-H. Commere, P. Jay, P. J. Sansonetti, The cytosolic bacterial peptidoglycan sensor Nod2 affords stem cell protection and links microbes to gut epithelial regeneration. *Cell Host Microbe* **371**, 792–798 (2014).
9. R. Cooney *et al*., NOD2 stimulation induces autophagy in dendritic cells influencing bacterial handling and antigen presentation. *Nat. Med.* **16**, 90–97 (2010).
10. L. H. Travassos *et al*., Nod1 and Nod2 direct autophagy by recruiting ATG16L1 to the plasma membrane at the site of bacterial entry. *Nat. Immunol.* **11**, 55–62 (2010).
11. B. Levine, N. Mizushima, H. W. Virgin, Autophagy in immunity and inflammation. *Nature* **469**, 323–335 (2011).
12. R. Ravindran *et al*., The amino acid sensor GCN2 controls gut inflammation by inhibiting inflammasome activation. *Nature* **531**, 523–527 (2016).
13. T. Saitoh *et al*., Loss of the autophagy protein Atg16L1 enhances endotoxin-induced IL-1β production. *Nature* **456**, 264–268 (2008).
14. T. Sato *et al*., Single Lgr5 stem cells build crypt-villus structures in vitro without a mesenchymal niche. *Nature* **459**, 262–265 (2009).
15. J. Lee *et al*., pH-dependent internalization of muramyl peptides from early endosomes enables Nod1 and Nod2 signaling. *J. Biol. Chem.* **284**, 23818–23829 (2009).
16. E. I. Azzam, J.-P. Jay-Gerin, D. Pain, Ionizing radiation-induced metabolic oxidative stress and prolonged cell injury. *Cancer Lett.* **327**, 48–60 (2012).
17. M. J. Rodríguez-Colman *et al*., Interplay between metabolic identities in the intestinal crypt supports stem cell function. *Nature* **543**, 424–427 (2017).
18. C. R. Homer *et al*., A dual role for receptor-interacting protein kinase 2 (RIP2) kinase activity in nucleotide-binding oligomerization domain 2 (NOD2)-dependent autophagy. *J. Biol. Chem.* **287**, 25565–25576 (2012).
19. T. Sato *et al*., Paneth cells constitute the niche for Lgr5 stem cells in intestinal crypts. *Nature* **469**, 415–418 (2011).
20. X. Yin *et al*., Niche-independent high-purity cultures of Lgr5$^+$ intestinal stem cells and their progeny. *Nat. Methods* **11**, 106–112 (2014).
21. A. Ferretta *et al*., Effect of resveratrol on mitochondrial function: Implications in parkin-associated familiar Parkinson's disease. *Biochim. Biophys. Acta* **1842**, 902–915 (2014).
22. S. E. Girardin *et al*., Nod2 is a general sensor of peptidoglycan through muramyl dipeptide (MDP) detection. *J. Biol. Chem.* **278**, 8869–8872 (2003).
23. J. Asano *et al*., Intrinsic autophagy is required for the maintenance of intestinal stem cells and for irradiation-induced intestinal regeneration. *Cell Rep.* **20**, 1050–1060 (2017).
24. Ö. H. Yilmaz *et al*., mTORC1 in the Paneth cell niche couples intestinal stem-cell function to calorie intake. *Nature* **486**, 490–495 (2012).
25. K. L. Tinkum *et al*., Fasting protects mice from lethal DNA damage by promoting small intestinal epithelial stem cell survival. *Proc. Natl. Acad. Sci. U.S.A.* **112**, E7148–E7154 (2015).
26. A. Nugud, D. Sandeep, A. T. El-Serafi, Two faces of the coin: Minireview for dissecting the role of reactive oxygen species in stem cell potency and lineage commitment. *J. Adv. Res.* **14**, 73–79 (2018).
27. N. Fujita *et al*., The Atg16L complex specifies the site of LC3 lipidation for membrane biogenesis in autophagy. *Mol. Biol. Cell* **19**, 2092–2100 (2008).
28. M. T. Sorbara *et al*., The protein ATG16L1 suppresses inflammatory cytokines induced by the intracellular sensors Nod1 and Nod2 in an autophagy-independent manner. *Immunity* **39**, 858–873 (2013).
29. L. Jostins *et al*.; International IBD Genetics Consortium (IIBDGC), Host-microbe interactions have shaped the genetic architecture of inflammatory bowel disease. *Nature* **491**, 119–124 (2012).
30. K. K. Khanna, S. P. Jackson, DNA double-strand breaks: Signaling, repair and the cancer connection. *Nat. Genet.* **27**, 247–254 (2001).
31. F. Barreau *et al*., CARD15/NOD2 is required for Peyer's patches homeostasis in mice. *PLoS One* **2**, e523 (2007).
32. M. D. Muzumdar, B. Tasic, K. Miyamichi, L. Li, L. Luo, A global double-fluorescent Cre reporter mouse. *Genesis* **45**, 593–605 (2007).
33. K. L. Conway *et al*., Atg16l1 is required for autophagy in intestinal epithelial cells and protection of mice from *Salmonella* infection. *Gastroenterology* **145**, 1347–1357 (2013).
34. N. Mizushima, A. Yamamoto, M. Matsui, T. Yoshimori, Y. Ohsumi, In vivo analysis of autophagy in response to nutrient starvation using transgenic mice expressing a fluorescent autophagosome marker. *Mol. Biol. Cell* **15**, 1101–1111 (2004).
35. D. H. Reikvam *et al*., Depletion of murine intestinal microbiota: Effects on gut mucosa and epithelial gene expression. *PLoS One* **6**, e17996 (2011).
36. K. E. de Visser *et al*., Developmental stage-specific contribution of LGR5(+) cells to basal and luminal epithelial lineages in the postnatal mammary gland. *J. Pathol.* **228**, 300–309 (2012).
37. H. J. Snippert, A. G. Schepers, G. Delconte, P. D. Siersema, H. Clevers, Slide preparation for single-cell-resolution imaging of fluorescent proteins in their three-dimensional near-native environment. *Nat. Protoc.* **6**, 1221–1228 (2011).